



Published in final edited form as:

Soft Matter. 2011 December 22; 8: 1934–1946. doi:10.1039/C2SM06391C.

Influence of Red Blood Cells on Nanoparticle Targeted Delivery in Microcirculation

Jifu Tan¹, Antony Thomas², and Yaling Liu^{1,2}

¹Department of Mechanical Engineering and Mechanics, Lehigh University, Bethlehem, PA 18015, USA

²Bioengineering program, Lehigh University, Bethlehem, PA 18015, USA

Abstract

Multifunctional nanomedicine holds considerable promise as the next generation of medicine that allows for targeted therapy with minimal toxicity. Most current studies on Nanoparticle (NP) drug delivery consider a Newtonian fluid with suspending NPs. However, blood is a complex biological fluid composed of deformable cells, proteins, platelets, and plasma. For blood flow in capillaries, arterioles and venules, the particulate nature of the blood needs to be considered in the delivery process. The existence of the cell-free-layer and NP-cell interaction will largely influence both the dispersion and binding rates, thus impact targeted delivery efficacy. In this paper, a particle-cell hybrid model is developed to model NP transport, dispersion, and binding dynamics in blood suspension. The motion and deformation of red blood cells is captured through the Immersed Finite Element Method. The motion and adhesion of individual NPs are tracked through Brownian adhesion dynamics. A mapping algorithm and an interaction potential function are introduced to consider the cell-particle collision. NP dispersion and binding rates are derived from the developed model under various rheology conditions. The influence of red blood cells, vascular flow rate, and particle size on NP distribution and delivery efficacy is characterized. A non-uniform NP distribution profile with higher particle concentration near the vessel wall is observed. Such distribution leads to over 50% higher particle binding rate compared to the case without RBC considered. The tumbling motion of RBCs in the core region of the capillary is found to enhance NP dispersion, with dispersion rate increases as shear rate increases. Results from this study contribute to the fundamental understanding and knowledge on how the particulate nature of blood influences NP delivery, which will provide mechanistic insights on the nanomedicine design for targeted drug delivery applications.

Keywords

particle-cell interaction; hybrid model; Brownian dynamics; NP dispersion; microcirculation; Immersed Finite Element Method; nanomedicine

I. Introduction

Nanoparticles (NPs) have been extensively studied in recent years as the next generation of drug carriers and imaging probes [1–8]. By applying nanotechnology in medicine, liposomes and polymer-drug conjugates based NPs provide various advantages over traditional drugs, such as targeted delivery, controllable release, dual imaging and therapeutic functions, etc. Several nanomedicines, such as liposome-encapsulated doxorubicin, liposomal amphotericin

*Corresponding author. Tel.: +1-610-758-5839; fax: +1-610-758-6224. yal310@lehigh.edu (Y. Liu).

B, liposomal morphine have been approved by US Food and Drug Administration (FDA)[9]. Properties of NP such as size, shape and surface chemistry play an important role in NP binding and clearance. Generally, particles bigger than 200 nm are efficiently filtered by liver, spleen and bone marrow, while particles smaller than 10 nm can be quickly cleared by the kidney or through extravasation [9–11]. To achieve targeted delivery, NPs are usually coated with ligands that bind specifically to a particular type of receptor on the cell surface [12]. NP targeted delivery in a vascular system involves the interplay of transport, hydrodynamic force, and multivalent interactions with targeted biosurfaces. First, NPs are margined from the blood stream to the vicinity of the vascular wall. The dispersion of particles in a fluid flowing through a tube can be described by the Taylor-Aris theory [13–14]. Then, the interaction of NPs with the vessel wall occurs when their minimum distance is below 20 nm [15–16]. The ligands on the NP surface bind with receptors on the vessel wall, leading to large adhesive forces. After initial binding, the NP may get firmly adhered or may be washed away, depending on the strength of binding, flow conditions, etc.

Blood is a complex biological fluid made of components such as red blood cells (RBC), monocytes, platelets, proteins, etc. When blood flows through vessels, the two-phase nature of the blood becomes important as the diameter of RBCs becomes comparable to the vessel diameter. Various unique phenomena have been observed in microcirculation due to the particulate nature of the blood, such as (a) vessel diameter dependent apparent viscosity: Fåhræus–Lindqvist effect; (b) existence of a cell-depleted layer near the wall: cell free layer; and (c) blunt velocity profile. These phenomena have significant impact on NP targeted delivery efficiency. First, targeted binding to diseased cells requires NPs to move close to the vascular wall, i.e. in a near wall binding-layer. Such a near wall binding-layer is coincident with the cell-free layer, with the addition of NPs in such layer. However, the thickness of such cell-free layer varies with vascular conditions, thus changes the binding properties. Second, the existence of blood cells in the core region of blood streams changes the NP dispersion rate through cell-NP interaction. Due to the small size of NPs, the dynamic delivery process, and the complex vascular environment, it is very challenging to explore these phenomena experimentally *in vivo*. Current theoretical studies in NP therapeutic delivery are limited to an ideal Newtonian flow in a 2D channel under shear flow[17–19] without blood cells, which can't reflect the behavior of particles under microcirculation. Thus, characterization of this process for different size of NPs under different vascular flow conditions through a mathematical model is crucial for elucidating NP binding *in vivo* [20], particularly to understand how interactions between blood cells and NPs influence the particle motion and binding.

This paper presents for the first time, the simulation results for dynamic transportation and adhesion of widely used polymer–drug conjugates based NPs in microcirculation using Brownian adhesion dynamics method coupled with cell model through the Immersed Finite Element Method (IFEM) platform[21–24]. The NP size and concentration are chosen based on the *in vivo* experiment data reported in literature. In the following sections of this paper, the NP adhesion kinetics theory and modeling method are described first. Then, adhesion processes for NPs under various conditions are presented. Next, the dispersion rate and binding rate of NPs are studied with and without RBCs considered. Finally, the conclusion and future work are presented.

II. Methods

A. Nanoparticle Brownian Adhesion Dynamics

Fundamental theories of Brownian dynamics indicate that random collisions from surrounding liquid molecules impact the motion of an immersed small particle[25–27]. The influence of Brownian motion on behaviors of NPs in microfluidic channel as well as

behaviors of platelets in blood flow has been studied[28–31]. For example, Mody *et al.*[28] used the platelet adhesive dynamics computational method to study the influence of Brownian motion of a platelet on its flow characteristics near a surface. Longest *et al.*[29] simulated the blood particle adhesion process in a non-parallel flow. Gentile *et al.*[30] studied the transport of NP in blood vessels under the effect of vessel permeability and blood rheology. Lee *et al.* [31] simulated a NP focusing lens in a microfluidic channel. Patankar *et al.* [32] proposed an algorithm for direct numerical simulation of Brownian motion by adding random disturbance in fluids. At microscale, the drag forces acting on particles such as blood cells are significantly large (> 50 pN for particle size > 1 μm), thus Brownian motion is negligible [28]. At nanoscale, Brownian force becomes a dominant force to drive NP near vascular wall surface, while the drag force acting on a NP is relatively small. For example, Shah *et al.*[33] used brownian dynamics to study the dynamic delivery process of nanorods and nanospheres under different shear rates. The random forces $\mathbf{R}(t)$ acting on a NP is responsible for Brownian motion and satisfies the fluctuation-dissipation theorem[34]:

$$\langle \mathbf{R}_i(t) \rangle = 0, \quad (1)$$

$$\langle \mathbf{R}_i(t) \mathbf{R}_j(t') \rangle = 2k_B T \beta_t \delta_{ij} \delta(t - t') \boldsymbol{\delta}, \quad (2)$$

where, $\boldsymbol{\delta}$ is the unit-second order tensor, δ_{ij} is the Kronecker delta, $\delta(t - t')$ is the Dirac delta function, $k_B T$ is thermal energy of system.

The friction coefficient depends on several physical parameters, such as fluid viscosity, size and shape of the NP. The friction coefficient for spherical particles can be easily derived from Stokes' law:

$$\beta_t = 3\pi \mu d \quad (3)$$

where μ is the fluid viscosity, d is the diameter of particle. The velocity of a particle moving under a deterministic force in a fluid with velocity \mathbf{V}_f is given by:

$$\mathbf{V}_p = \left(\frac{\mathbf{F}_{\text{det}}}{\beta_t} + \mathbf{V}_f \right) (1 - e^{-\frac{\beta_t}{m}t}) \quad (4)$$

where \mathbf{V}_p and \mathbf{V}_f are the particle and fluid velocity vectors, respectively; \mathbf{F}_{det} is the total deterministic force acting on the NP (including Brownian force, adhesion force, etc.):

$$\mathbf{F}_{\text{det}} = \mathbf{R}(t) + \mathbf{F}_{\text{cell-NP}} + \mathbf{F}_{\text{ad}} + \mathbf{F}_{\text{NP-NP}} \quad (5)$$

where $\mathbf{R}(t)$ is the random force, \mathbf{F}_{ad} is the adhesive force from ligand-receptor bonds; $\mathbf{F}_{\text{cell-NP}}$ is cell-NP interaction force, $\mathbf{F}_{\text{NP-NP}}$ is NP-NP interaction force. The detailed formulation for ligand-receptor binding can be found in our previous publication[33], cell-NP and NP-NP interaction forces are presented in Section C.

For a time step (usually ~ 1 μs) much greater than characteristic time constant m/β_t (~ 10 ns), the NP moves with a terminal velocity, thus Eq. (4) reduces to:

$$\mathbf{V}_p = \frac{\mathbf{F}_{\text{det}}}{\beta_t} + \mathbf{V}_f \quad (6)$$

Eq. (6) actually describes that the deterministic force acting on a particle is balanced by the drag force from the fluid. This is reasonable since the mass of a NP is so small that inertia

effect can be neglected. This terminal velocity is then used to update the NP position in

translational direction. The ratio between $\frac{\mathbf{F}_{\text{det}}}{\beta_f}$ and \mathbf{V}_f varies from tens to thousands, depending on whether NP is in free suspension, under collision with cells, or binding on the wall.

B. Red Blood Cell and Fluid-Structure Interaction Model

In the simulation, RBCs are modeled as flexible thin membranes enclosing a fluid [35–36], as shown in Figure 1. Both the cytoplasm inside the RBC and the blood plasma outside the RBC have a viscosity of around 0.01 dyn-s/cm, thus are treated as the same fluid. A Mooney–Rivlin strain energy function similar to that of our previous work[35–36] and others[37–39], is used to depict the material behavior of the RBC membrane:

$$W=C_1 (I_1 - 3)+C_2 (I_2 - 3) \quad (7)$$

with the material properties specified by constants C_1 and C_2 . I_1 and I_2 are the functions of the invariants of the Cauchy-Green deformation tensor \mathbf{C} .

RBCs and their interaction with fluid flow are modeled by the IFEM formulation[35–36]. The IFEM was developed by Zhang *et al.* and Liu *et al.*[21–23, 40] to solve coupled fluid-structure interaction problems. Because much of the method has been derived in detail in works[21–23, 40], we will just briefly list out the IFEM procedures below, and refer the interested reader to those for further details. The fluid in the simulation is assumed to be an incompressible viscous fluid governed by the Navier–Stokes equations:

$$\rho \left(\frac{\partial \mathbf{v}_f}{\partial t} + \mathbf{v}_f \cdot \nabla \mathbf{v}_f \right) = -\nabla p + \mu \nabla^2 \mathbf{v}_f \quad (8)$$

$$\nabla \cdot \mathbf{v}_f = 0 \quad (9)$$

where \mathbf{v}_f is the fluid velocity in the fluid domain. Motivated by Peskin's immersed boundary method [41–43], as in IFEM[40], an extra volumetric force is introduced to avoid the complex re-meshing usually encountered in the fluid-structure interaction problems. This extra force \mathbf{F}^{FSI} , called the fluid-structure interaction force, is defined as:

$$\mathbf{F}^{\text{FSI}} = \begin{cases} -(\rho^s - \rho^f) (\dot{\mathbf{v}}^s - \mathbf{g}) + \nabla \cdot (\boldsymbol{\sigma}^s - \boldsymbol{\sigma}^f), & \text{in } \Omega^s \\ 0, & \text{in } \Omega \setminus \Omega^s \end{cases} \quad (10)$$

where \mathbf{v} is the velocity, ρ is the density and $\boldsymbol{\sigma}$ is the Cauchy stress tensor. s and f donate for solid and fluid respectively.

For a Newtonian fluid of uniform viscosity, $\boldsymbol{\sigma}^f$ can be written as:

$$\boldsymbol{\sigma}^f = -p^f \mathbf{I} + \mu \left[\nabla \mathbf{v}^f + (\nabla \mathbf{v}^f)^T \right] \quad (11)$$

where μ is the fluid viscosity and p^f is the hydrostatic pressure.

To interpolate between the Eulerian and Lagrangian domains, a restriction operator L_t^s from Ω onto Ω^s is needed to make the system complete:

$$(L_{\Omega_t^s} \psi)(\mathbf{X}, t) \equiv \psi(\mathbf{x}(\mathbf{X}, t), t), \forall \mathbf{X} \in \Omega_0^s \quad (12)$$

With this mapping function, we obtain the solid velocity and displacement from the Eulerian space as:

$$\mathbf{v}^s = L_t^s \mathbf{v}, \text{ in } \Omega^s \quad (13)$$

$$\frac{\partial \mathbf{u}^s}{\partial t} = \mathbf{v}^s, \text{ in } \Omega^s \quad (14)$$

Eq. (13) basically interpolates the solid velocity from the fluid field through a mapping function.

The coupled fluid-structure interaction equations are solved through finite element method. The weak forms of the immersed system and other details can be found in previous publication [40]. To reduce numerical oscillations, the velocity test function is employed along with stabilization parameters. Using integration by parts and the divergence theorem, the Petrov-Galerkin weak form is obtained. Then, the nonlinear system is solved using the Newton-Raphson method. Moreover, Generalized Minimum Residual (GMRES) iterative algorithm is employed to improve computation efficiency and to compute residuals based on matrix-free techniques[44].

C. Particle-Particle and Particle-Cell Interaction Model

A schematic illustration for Particle-cell interaction is given in Figure 2. The motion of NPs is governed by Brownian adhesion dynamics [7]. As described in Section B, RBCs and their interaction with fluid flow is modeled by IFEM formulation [35–36]. For NPs, a Lennard-Jones potential is introduced to characterize the interaction between individual particles.

$$V(r) = 4\epsilon \left[\left(\frac{\sigma}{r} \right)^{12} - \left(\frac{\sigma}{r} \right)^6 \right] \quad (15)$$

$$F(r) = - \frac{dV(r)}{dr} = \frac{24\epsilon}{\sigma} \left[2 \left(\frac{\sigma}{r} \right)^{13} - \left(\frac{\sigma}{r} \right)^7 \right] \quad (16)$$

where σ is the distance at which the energy is zero, ϵ is the strength of the potential energy.

A short-range repulsive Morse potential is used to avoid overlapping between NPs and RBCs:

$$\phi(r) = D_e \left[e^{2\beta(r_0-r)} - 2e^{\beta(r_0-r)} \right] \quad (17)$$

$$f(r) = - \frac{\partial \phi(r)}{\partial r} = 2D_e \beta \left[e^{2\beta(r_0-r)} - e^{\beta(r_0-r)} \right] \quad (18)$$

where r_0 and D_e stand for the zero force length and surface energy respectively, and β is a scaling factor. Similar cell-particle collision model has been used by Almomani *et al.* [45] to study the erythrocyte-platelet interaction in blood flow, where the collision forces were modeled as spring forces between the surfaces of the colliding particles and erythrocytes. The parameters used in the simulation model are listed in Table 1.

It should be noticed that different time steps are used to track particle motion and blood cell deformation, i.e., a smaller time step dtt for NPs and a larger time step dt for blood cell-fluid interaction, as shown in Figure 3A and 3B. The time steps are determined by the flow velocity and the particle diffusion speed. A small time step is needed to capture the high speed Brownian motion while a larger time step can be used for relatively slow RBC-fluid interaction. Similar different time steps had been used to capture the many-particle binding dynamics with a receptor coated surface by Ariei *et al.*[46].

However, a few problems may arise due to the usage of varied time stepping. When NPs approach the RBCs, the shortest distance L_s between NPs and the RBCs' surface is calculated and compared with a cut-off distance R_{cut} defined for implementation of Morse potential. For $L_s < R_{cut}$, the Morse potential applies a repulsive force so that NPs can be repelled away. However, the particles may penetrate into the RBCs if the distance the RBCs travel per time dt is larger than R_{cut} which usually happens unless a very small flow velocity is applied. To resolve this problem, the time step for RBCs dt is divided into a number of equally small time step dtt , as shown in Figure 3C, and the RBC position virtual images at intermediate time intervals are interpolated by:

$$d^s(t_1+i*dtt)=d^s(t_1)+\frac{d^s(t_1+dt)-d^s(t_1)}{dt} \times i \times dtt \quad (19)$$

Such virtual images for RBCs are established only for cell-particle repulsive force calculation. In the simulation, R_{cut} is chosen as 400 nm. If the fluid velocity is 40 $\mu\text{m/s}$, to avoid particle penetration, the maximum time step is 0.01s. However, during 0.01s, NP travels 296 nm due to Brownian motion. Due to the exponential form of Morse potential and power form of Lennard-Jones potential, such big distance per time step will generate huge repulsive forces. To be safe, dtt is chosen as 0.00001s, under which NP travels around 9 nm each time step. In summary, the position of RBCs is updated based on larger time step dt while NPs positions are updated on smaller time step dtt . The collision between the RBCs and NPs are captured by RBC virtual images at intermediate steps. Such two time step algorithm will largely increase the simulation speed without losing accuracy.

D. Nanoparticle dispersion coefficient calculation

NP dispersion coefficient will be calculated under various flows conditions. The dispersion coefficient can be evaluated by tracking the motion of NPs and calculate the mean square displacements [47–49]. Since margination process is important in nanoparticle attachment to vascular wall and drug delivery, we focus on the particle dispersion in the radial direction. The mean square displacement (MSD) is defined as

$$\langle \xi(t, \tau) \rangle = \frac{1}{N_c} \sum_{i=1}^{N_c} \frac{1}{N} \sum_{\alpha=1}^N [r_i^\alpha(\tau+t) - r_i^\alpha(\tau)]^2 \quad (20)$$

where $r_i^\alpha(\tau+t)$ is the radial-coordinate of particle α from initial configuration i at time t starting from τ . N is the total number of particles, N_c is the total number of simulation runs. τ is chosen to be large enough so that there is no dependence on the initial particle distribution. Then the Overall Diffusion Coefficient (ODC) can be obtained by

$$D(t, \tau) = \frac{1}{2} \frac{d}{dt} \langle \xi(t, \tau) \rangle \quad (21)$$

It should be noted that NPs dispersion in blood vessel is not a free diffusion process because NPs have instantaneous collisions with the RBCs and vessel wall. In this sense, the mean square displacement defined before cannot truly reflect the distance NPs traveled at each time step. Thus to better reflect the interaction of RBCs on NP diffusion, Instantaneous Diffusion Coefficient (IDC) is defined as

$$\langle \xi(dtt) \rangle = \frac{1}{N_c} \sum_{i=1}^{N_c} \frac{1}{N} \sum_{\alpha=1}^N [r_i^\alpha(t+dtt) - r_i^\alpha(t)]^2 = 2D_I dtt \quad (22)$$

where dtt is the small time step, D_I is the Instantaneous Diffusion Coefficient, $\langle \xi(dtt) \rangle$ is the Instantaneous Mean Square Displacement (IMSD).

III. Simulation Results

Since RBCs consist of almost 50% of the blood and are dominant over all other blood cells, only RBCs and NPs are modeled in the simulation. The combined Immersed Finite Element and particle Brownian dynamics model is used to model the NPs delivery process in microcirculation.

The number of RBCs inside the simulation domain is determined by the volume ratio of RBC to blood to achieve a RBC concentration close to the hematocrit of human blood (normally in the range of 30–55% in larger arteries and drops to 10–15% in capillaries[50]). In our simulation, a number of RBCs are put into the fluid domain to reach a hematocrit of around 36%. NP size is chosen between 10~200 nm, which is the recommended range reported in literature [9–11]. PLGA-PEG-COOH NP suspension of 10 $\mu\text{g}/\mu\text{L}$ [3] has been used to target cancer *in vivo*. Paclitaxel-loaded TPGS-emulsified PLGA NPs with concentration of 10 mg/mL[4] were studied both *in vitro* and *in vivo*. Antitubercular drugs loaded PLG-NP with concentration of 25 mg/2 mL [5] showed strong potential against murine tuberculosis. The concentrations mentioned above are the injection concentration. In our work, considering that NPs are diluted in blood flow during circulation, a lower concentration of 1 $\mu\text{g}/\mu\text{L}$ is chosen as the NP concentration at the target disease site. Periodic boundary conditions are applied to the left and right side of boundaries so that RBCs and NPs exit from one end of the channel can re-enter the inlet. Based on Einstein–Stokes equation, theoretical diffusion coefficient for the NPs with a diameter of 100 nm is $2.2 \times 10^{-8} \text{ cm}^2/\text{s}$. The average flow rate in the channel is 20 $\mu\text{m}/\text{s}$, which is within physiological speed range from 10–100 $\mu\text{m}/\text{s}$ for capillary vessel with diameter between 10 and 20 μm [54].

In the simulations, two independent sets of meshes are used for RBCs and fluid domain. Each Red blood cell consists of 1534 nodes and 4340 elements. The fluid mesh has 5705 nodes and 16632 elements. A time step of 0.00001 s and 0.002 s are used for the NP Brownian dynamics and RBCs-fluid interaction simulations, respectively. To clearly illustrate both NPs and RBCs, cross-sectional views are used in the simulation snapshots throughout this paper.

To explore the effect of RBCs on NP delivery, three sets of simulation setups are used: pure particles, particles mixed with RBCs to keep the total amount of particle same as pure particle case, and particles mixed with RBC to keep the same effect concentration excluding RBC volume, as shown in Figure 4. The pure particle case is used as a control. The second case is used to check the influence of RBCs on particle dispersion and binding if the same dosage of NPs is considered. The third case is used to check the influence of RBCs on particle dispersion and binding if volume exclusion effect of the RBCs is removed, thus the effective particle concentration is the same as the pure particle case. It should be noticed that

NP suspension might increase the effective viscosity of blood. However, in this work, the NP volume concentration is around 0.08%, based on the results reported by Lee *et.al.*[55], the enhancement of NP on viscosity is less than 1% under such low concentration, thus the viscosity enhancing effect by NP could be ignored in our simulations.

A. Verification of NP diffusion coefficient with Taylor-Aris theory

When NPs are injected into the blood flow, they spread out across the vessel under the combined effects of diffusion and fluid flow. It is derived analytically that the particle concentration generated is centered on a point which moves with the mean speed of flow and is symmetrical about this point in spite of the asymmetry of the flow[14], as shown in Figure 5. The diffusion coefficient for NPs with a diameter of 100 nm is $2.2 \times 10^{-8} \text{ cm}^2/\text{s}$. By tracking the position of the NPs in fluid flow direction, the diffusion can be calculated by MSD:

$$\langle \xi(dtt) \rangle = \frac{1}{N_c} \sum_{i=1}^{N_c} \frac{1}{N} \sum_{\alpha=1}^N [x_i^\alpha(t+dtt) - x_i^\alpha(t) - V_i^\alpha dtt]^2 = 2D_x dtt \quad (23)$$

where V_i^α is the velocity of particle α at time step i , D_x is the diffusion in fluid flow direction indicated by X .

The observed MSD is a quadratic function of t since the displacement contains axial displacement term $V_i^\alpha t$, as shown in Figure 5A. To eliminate the tube flow effect on NPs distribution, Eqn. (23) is used to obtain the diffusion coefficient in x direction. By linear data fitting, average $\text{IMSD} < \xi(dtt) > = 4.38 \times 10^{-10} \text{ cm}^2$, as indicated by a dash line in Figure 5B.

Thus, the diffusion coefficient is $D_x = \frac{\langle \xi(dtt) \rangle}{2dtt} = 2.19 \times 10^{-8} \text{ cm}^2/\text{s}$, which agrees with the theoretical value.

B. The influence of shear rate on nanoparticle delivery

The influence of different shear rates on nanoparticle delivery is considered first. The shear rate is determined by the velocity of the blood flow and vessel diameter. Typically in capillary with size between 10 and 20 μm in diameter, the mean velocity of blood flow usually ranges from 10 $\mu\text{m}/\text{s}$ to 100 $\mu\text{m}/\text{s}$ [54], and the maximum shear rate at the vessel wall ranges from 8 to 40 s^{-1} . In the simulation model, the effect of RBC tumbling motion on the dispersion of NPs under the shear rate of 8 s^{-1} and 16 s^{-1} are considered. To study how RBCs influence the delivery of nanoparticles of different size, two types of NPs with size 10 nm and 100 nm are studied, which are within the recommended size range (10~200 nm) of tumor drug carriers. A snap shot of the model is shown in Figure 6.

RBC tumbling motion is found to help the dispersion of the NPs from the core region toward the edge of the simulation domain, as shown in Figure 6. Once RBCs tumble under shear flow, NPs begin to redistribute along with the motion of the RBCs. Compare to the case with pure NPs, the NP distribution when mixed with RBCs is not uniform, with more NPs in the near vessel wall region. Such non-uniform NP distribution, as shown in Figure 7, is favorable for NPs targeted binding and subsequently leads to higher NP binding efficacy, which will be discussed Section C. From Figure 7A, it is shown that with RBCs, the number of NPs in the edge region increases from 5% to 10%, almost doubled compared to that without RBCs. Such non-uniform NP distribution is induced by the RBCs volumetric exclusion and tumbling effect. Similar increased near-wall high particle concentration has also been reported for platelet distribution in capillary flow[56–59].

Besides distribution, RBCs also influence NPs dispersion. The existence of RBCs serves as dual roles to the particle dispersion. On one hand, due to the interaction between the cells and the particles, the particles will be pushed around as RBCs tumble in the blood, thus lead to higher dispersion coefficient. For example, when 100 nm diameter NPs are introduced in the model under a shear rate of 8 s^{-1} , the average dispersion coefficient (half of the slope of the mean square displacement) is $3.6 \times 10^{-8} \text{ cm}^2/\text{s}$, a significant increase compared to the theoretical value of $2.2 \times 10^{-8} \text{ cm}^2/\text{s}$ without RBCs considered, as shown in Figure 8A. Such enhanced dispersion is also observed by Crowl *et al.* [57] on platelet motion induced by red blood cells. On the other hand, RBCs trap particles in the space in between, especially for small NPs which diffuse faster than RBCs rotation. For example, the trapping effect for 10 nm particles is dominant during the first 0.7s when RBCs/NPs mixture are placed under a shear flow; however, the diffusion enhancement effect outweighs trapping effect once the RBCs tumbling become apparent, which is reflected in Figure 8B where the average dispersion coefficient with RBCs is $9.3 \times 10^{-8} \text{ cm}^2/\text{s}$ as compared to $6.4 \times 10^{-8} \text{ cm}^2/\text{s}$ without RBCs. It should be noted that the dispersion coefficient without RBCs is smaller than the theoretical free diffusion value $2.2 \times 10^{-7} \text{ cm}^2/\text{s}$ due to the constrained effect at the fluid channel boundaries. The zoom-in sub-plot of the MSD at the beginning (Figure 8B) shows that the dispersion coefficient is close to the theoretical value of free diffusion. To eliminate the constrained effect, the instantaneous diffusion coefficients (IDC) is calculated based on Eqn.(22). It is shown in Figure 8C that IDCs are very close to the theoretical value of NPs of corresponding size. For example, for 100 nm NPs, the IDC with RBCs is $2.22 \times 10^{-8} \text{ cm}^2/\text{s}$, while the IDC without RBCs is $2.20 \times 10^{-8} \text{ cm}^2/\text{s}$, as shown in Figure 8C. Similar results were also observed for 10 nm NPs, as shown in Figure 8D.

The diffusion coefficient of particles is a physical property which usually should not change with shear rates. However, the dispersion rate might be influenced by the existence of RBCs and change with shear rates. The dispersion rate of NPs is characterized at different shear rates in our simulations. With RBCs, as the shear rate increases, the mean square displacement for NPs increases for both 100 nm and 10 nm diameter NPs, as shown in Figure 9. This is explained by the fact that RBCs tumbles faster at higher shear rates, thus push the surrounding NPs and lead to larger dispersion. The enhancement in dispersion rate due to the existence of RBCs is more apparent for 100 nm NPs compared to 10 nm NPs. However, without RBCs, no matter how much the shear rate increases, the dispersion coefficients for NPs almost keep unchanged. Thus, larger shear rate enhances NPs dispersion due to the faster rotation of RBCs, which is favorable for NPs margination toward vessel wall surface.

C. The influence of RBCs on NP binding

NP binding dynamics involves molecular level binding between ligands coated on the NP surface and receptors on the vessel wall. The detailed binding adhesion dynamics of individual particles of arbitrary shape under various flow conditions has been studied in our previous work[33]. In this paper, we focus on collective behavior of NPs under the influence of RBCs, thus simply bind NPs upon its contact with the wall surface. As described in Section B, the existence of RBCs lead to high near-wall NP concentration and is expected to induce faster NP binding. The NP binding dynamics is studied in a $20 \mu\text{m}$ wide vessel with the existence of RBCs under an average inlet flow rate of $20 \mu\text{m}/\text{s}$. With RBCs, the particle distribution is not uniform (see Figure 10A and B), particularly with more particles in the near vessel wall region. This nonuniform particle distribution is favorable for NPs targeted binding because with high concentration in the cell free layer region, more particles are likely to bind to the diseased area.

The NPs binding time history is plotted in Figure 11. For the same NP concentration case, there are fewer NPs in the simulation domain, thus the total number of bounded NPs with

the existence of RBCs is less than that without RBCs. However, the NPs binding rate in the initial stage with the existence of RBCs is higher than that without RBCs, as shown in Figure 11A. For the same NP dosage case, since the NP density at the near wall region is much higher than that without RBCs, NPs with RBCs bind at a significantly higher rate than that without RBCs, as shown in Figure 11B. In Figure 11, the number of bonded NPs gradually reaches a plateau, which indicates that NP binding is a diffusion limited reaction process and the number of free NPs decreases over time.

For quantitative calculation of the binding rate, a first order reaction model is used to fit the binding curve to retrieve the binding rate:

$$\frac{\partial N_b}{\partial t} = K_f(N_0 - N_b) \quad (24)$$

where N_b is the number of bonds, N_0 is the total number of NPs in the fluid domain, K_f is the forward binding rate with units of 1/s.

The analytical solution for Eqn.(24) is $N_b = N_0 (1 - \exp(-K_f t))$

However, if the bonds formation is diffusion or reaction limited, the kinematics of bonds formation is not exponential function of time. Douglas *et al.*[60] proposed to use a non-exponential reaction rate to express the bonds formation, which can be modified as:

$$N_b = N_0 (1 - \exp[-K_f t]^\beta) \text{ where } \beta \text{ is a parameter related to the time dependent rate.}$$

The same method is also used by Park *et al.*[61] to fit the data of non-equilibrium NP adsorption on a model biological substrate. By fitting the data obtained in NPs binding time history, the binding rates with RBCs, without RBCs, under the same density, and under the same dosage are summarized in Figure 12.

As shown in Figure 10, with RBCs, the percentage of particles in the cell free layer increase from 5% to 10%, almost doubled compared to that without RBCs. This favorable particle distribution leads to more than two times higher binding efficacy for NPs with RBCs compared to that without RBCs, as shown in Figure 12. This higher binding rate is likely induced by the tumbling and blocking effect of RBCs which can help increase the NP density in the cell free layer. The particles enter the cell free layer cannot easily diffuse back to the core region of the vessel filled with RBCs. While without RBCs, the particles are free to diffuse in any direction, consequently, the binding rate without RBCs is decreased.

D. NP delivery in small capillaries

The NPs delivery process is also studied in a small capillary with a diameter of 11 μm . The configuration of the model is shown in Figure 13, with cells aligned inside the channel in a linear profile. Figure 14 shows that the NP concentration is higher in the near wall region with RBCs while the NP concentration is uniform across the capillary without RBCs. The higher NP concentration in the cell free layer leads to a larger binding rate compared to those NPs without RBCs, as shown in binding time history in Figure 15. For NPs without RBCs, the binding rate does not change with flow rate, thus only the NP binding time history under 20 $\mu\text{m/s}$ is plotted in Figure 15A. The binding rate is also influenced by particle size. For example, binding rate for NPs with a diameter of 100 nm is larger than NP with a diameter of 200 nm due to the faster diffusion, as shown in Figure 15B. The binding rates are calculated by exponential fitting of binding time history and are summarized in Figure 15C–D. The NP binding rates with RBCs are always larger than that without RBCs. The binding rate increases with decreased particle size. For NPs with RBCs, the binding rate increases slightly when the average flow speed increases from 20 $\mu\text{m/s}$ to 50 $\mu\text{m/s}$. Similar

experimental results showing that flow rate minimally influence NP binding have been reported by Haun *et al.* [62] in a flow chamber test.

IV. Experimental validation

Microfluidic based blood vessel mimicking devices have been successfully applied in our lab to study NP transport and distribution[63]. To verify the results obtained in the simulation, experimental study on NPs distribution was performed by flowing 100 nm fluorescence NPs through a microfluidic channel of width 20 μm . In brief, straight 20 μm wide microfluidic channels were fabricated using standard soft lithography process[64]. The PDMS microfluidic device was bonded on clean glass slides after treating in an oxygen plasma chamber. The surface of the PDMS device was then functionalized with NeutrAvidin to bind with the biotin coated NPs. A mixture of RBCs and 100 nm biotin coated NPs with volume ratio of 36% was injected into the microfluidic device using a Harvard PHD 2000 syringe pump. The same flow rate used the simulation was chosen (20 $\mu\text{m/s}$). Channels were flushed with Phosphate Buffered Saline to remove unbound NPs from the channel after NPs distribution reached an equilibrium. Imaging was done using a fluorescent microscope (Olympus IX81). After eliminating the background noise and normalizing the fluorescence intensity with the total intensity, the fluorescence intensity distribution of NPs across the channel is analyzed and plotted in Figure 16A. It is observed that the NP fluorescent intensity is higher near the channel wall compared to the core region, which is consistent with the simulated NPs distribution profile shown in Figure 16B. As a control case, flux of pure NPs without RBCs was also performed, as shown in Figure 16C. The NP fluorescent intensity profile is flat across the channel, which again agrees with the simulation results shown in Figure 16D. It should be noted that NP fluorescent intensity is not exactly NP concentration. Due to the small size of the NPs and high flow rate, individual NPs are very hard to be visualized even with high-speed spinning disk confocal microscope. However, it is believed that NP fluorescence intensity profile essentially reflect the characteristics of the NPs distribution. Comparing the simulation and experiment data, it is concluded that RBCs can enhance the NP concentration in the margin of the vessels, thus leads to higher binding rate.

V. Discussions and summary

The enhanced NP dispersion and binding with the existence of RBCs observed in our simulations is believed to be not only a volume exclusion effect. We have shown that NP binding rate is higher for both RBC mixed with NPs of the same dosage and effective concentration compared to pure NPs cases. Such enhanced NP binding is directly induced by the higher concentration of NPs near the vessel wall, which indicates that NPs originally located in the center of the vessel will migrate toward the vessel edge during their collisions with the RBCs. To illustrate this dynamic migration process, trajectories of four NPs are tracked and analyzed in the simulation and illustrated in Figure 17. Two NPs in the core region (NP2 and NP3) are observed to migrate toward the edge of the channel. During the same period, two NPs in the edge (NP1 and NP4) are found difficult to diffuse toward the center due to the existence of RBCs moving in a relatively higher velocity in the core region.

In summary, a particle-cell hybrid model is developed to model NPs transport, dispersion, and adhesion dynamics in blood stream through coupled Immersed Finite Element method and particle Brownian adhesion dynamics. The dispersion and adhesion kinetics of NPs in microcirculation is studied for the first time with cell hydrodynamics coupled with particle Brownian dynamics. The adhesion kinetics of NPs is found to be significantly influenced by the existence of RBCs and shear rates. The cell-free-layer and NP-cell interaction largely influence both the dispersion and binding rates, thus impact targeted delivery efficacy.

Under a shear flow, the RBCs' tumbling motion will enhance NP dispersion. This leads to an increase in NP dispersion rate with increased shear rate. The distribution of NPs in capillary flow is not uniform, with more particles near the vessel wall surface. Such margination of NPs occurs due to hydrodynamic interaction and RBCs volumetric exclusion effect. Higher density of NPs in the near-wall region leads to higher binding rate for NPs in both 20 μm and 11 μm capillaries. The binding rate of NPs with RBCs is two times of that without RBCs. This observation is applicable to NPs of various sizes from 10 nm to 200 nm. Results from this study contribute to the fundamental understanding and knowledge on how the particulate nature of blood influences NP delivery, which will provide mechanistic insights on the nanomedicine design for targeted drug delivery applications.

Acknowledgments

The authors acknowledge the supports of this work from National Science Foundation (NSF) CAREER grant CBET-1113040, NSF CBET-1067502, and National Institute of Health (NIH) grant EB009786.

REFERENCE

1. Chauvierre C, et al. Novel polysaccharide-decorated poly(isobutyl cyanoacrylate) nanoparticles. *Pharmaceutical Research*. 2003; 20(11):1786–1793. [PubMed: 14661923]
2. Farokhzad OC, Langer R. Nanomedicine: Developing smarter therapeutic and diagnostic modalities. *Advanced Drug Delivery Reviews*. 2006; 58(14):1456–1459. [PubMed: 17070960]
3. Mathiowitz E, et al. Biologically erodable microsphere as potential oral drug delivery system. *Nature*. 1997; 386(6623):410–414. [PubMed: 9121559]
4. Nasongkla N, et al. Multifunctional polymeric micelles as cancer-targeted, MRI-ultrasensitive drug delivery systems. *Nano Letters*. 2006; 6(11):2427–2430. [PubMed: 17090068]
5. Peppas NA. Intelligent biomaterials as pharmaceutical carriers in microfabricated and nanoscale devices. *Mrs Bulletin*. 2006; 31(11):888–893.
6. Roney C, et al. Targeted nanoparticles for drug delivery through the blood-brain barrier for Alzheimer's disease. *Journal of Controlled Release*. 2005; 108(2–3):193–214. [PubMed: 16246446]
7. Shah P. Use of nanotechnologies for drug delivery. *Mrs Bulletin*. 2006; 31(11):894–899.
8. Sukhorukov GB, Mohwald H. Multifunctional cargo systems for biotechnology. *Trends in Biotechnology*. 2007; 25(3):93–98. [PubMed: 17207546]
9. Petros RA, DeSimone JM. Strategies in the design of nanoparticles for therapeutic applications. *Nat Rev Drug Discov*. 2010; 9(8):615–627. [PubMed: 20616808]
10. Alexis F, et al. Factors Affecting the Clearance and Biodistribution of Polymeric Nanoparticles. *MOLECULAR PHARMACEUTICS*. 2008; 5(4):505–515. [PubMed: 18672949]
11. Wang J, et al. More Effective Nanomedicines through Particle Design. *Small*. 2011; 7(14):1919–1931. [PubMed: 21695781]
12. Lutters BCH, et al. Blocking endothelial adhesion molecules: a potential therapeutic strategy to combat atherogenesis. *Current Opinion in Lipidology*. 2004; 15(5):545–552. [PubMed: 15361790]
13. Aris R. On the dispersion of a solute in a fluid flowing through a tube. *Proceedings of the Royal Society of London Series A-Mathematical and Physical Sciences*. 1956; 235(1200):67–77.
14. Taylor G. Dispersion of Soluble Matter in Solvent Flowing Slowly through a Tube. *Proceedings of the Royal Society of London, Series A-Mathematical and Physical Science*. 1953; 219(1137):186–203.
15. Dembo M, et al. The Reaction-Limited Kinetics of Membrane-to-Surface Adhesion and Detachment. *Proceedings of the Royal Society of London Series B-Biological Sciences*. 1988; 234(1274):55–83.
16. Dong C, et al. Mechanics of leukocyte deformation and adhesion to endothelium in shear flow. *Annals of Biomedical Engineering*. 1999; 27(3):298–312. [PubMed: 10374723]
17. Decuzzi P, Ferrari M. The adhesive strength of non-spherical particles mediated by specific interactions. *Biomaterials*. 2006; 27(30):5307–5314. [PubMed: 16797691]

18. Decuzzi P, et al. A theoretical model for the margination of particles within blood vessels. *Annals of Biomedical Engineering*. 2005; 33(2):179–190. [PubMed: 15771271]
19. Decuzzi P, et al. Adhesion of microfabricated particles on vascular endothelium: A parametric analysis. *Annals of Biomedical Engineering*. 2004; 32(6):793–802. [PubMed: 15255210]
20. Sanhai WR, et al. Seven challenges for nanomedicine. *Nat Nano*. 2008; 3(5):242–244.
21. Zhang L, et al. Immersed finite element method. *Computer Methods in Applied Mechanics and Engineering*. 2004; 193(21–22):2051–2067.
22. Liu WK, et al. Immersed finite element method and its applications to biological systems. *Computer Methods in Applied Mechanics and Engineering*. 2006; 195(13–16):1722–1749. [PubMed: 20200602]
23. Liu WK, Kim DW, Tang SQ. Mathematical foundations of the immersed finite element method. *Computational Mechanics*. 2007; 39(3):211–222.
24. Lee TR, et al. Immersed finite element method for rigid body motions in the incompressible Navier-Stokes flow. *Computer Methods in Applied Mechanics and Engineering*. 2008; 197(25–28):2305–2316.
25. Einstein, A. *Investigations on the Theory of Brownian Movement*. New York: Dover; 1956.
26. Ermak DL, Mccammon JA. Brownian Dynamics with Hydrodynamic Interactions. *Journal of Chemical Physics*. 1978; 69(4):1352–1360.
27. Li A, Ahmadi G. Dispersion and Deposition of Spherical-Particles from Point Sources in a Turbulent Channel Flow. *Aerosol Science and Technology*. 1992; 16(4):209–226.
28. Mody NA, King MR. Influence of Brownian motion on blood platelet flow behavior and adhesive dynamics near a planar wall. *Langmuir*. 2007; 23(11):6321–6328. [PubMed: 17417890]
29. Longest PW, Kleinstreuer C. Comparison of blood particle deposition models for non-parallel flow domains. *Journal of Biomechanics*. 2003; 36(3):421–430. [PubMed: 12594990]
30. Gentile F, Ferrari M, Decuzzi P. The transport of nanoparticles in blood vessels: The effect of vessel permeability and blood rheology. *Annals of Biomedical Engineering*. 2008; 36(2):254–261. [PubMed: 18172768]
31. Lee TR, et al. Numerical Simulation of a Nanoparticle Focusing Lens in a Microfluidic Channel by Using Immersed Finite Element Method. *Journal of Nanoscience and Nanotechnology*. 2009; 9(12):7407–7411. [PubMed: 19908798]
32. Sharma N, Patankar NA. Direct numerical simulation of the Brownian motion of particles by using fluctuating hydrodynamic equations. *Journal of Computational Physics*. 2004; 201(2):466–486.
33. S.Shah YL. Modeling Particle Shape-Dependent Dynamics in Nanomedicine. *Journal of Nanoscience and Nanotechnology*. 2011; 11(2):919–928.
34. Mori N, Kumagai M, Nakamura K. Brownian dynamics simulation for suspensions of oblong-particles under shear flow. *Rheologica Acta*. 1998; 37(2):151–157.
35. Liu YL, Liu WK. Rheology of red blood cell aggregation by computer simulation. *Journal of Computational Physics*. 2006; 220(1):139–154.
36. Liu YL, et al. Coupling of Navier-Stokes equations with protein molecular dynamics and its application to hemodynamics. *International Journal for Numerical Methods in Fluids*. 2004; 46(12):1237–1252.
37. Skalak R, et al. Mechanics of Rouleau Formation. *Biophysical Journal*. 1981; 35(3):771–781. [PubMed: 7272459]
38. Eggleton CD, Popel AS. Large deformation of red blood cell ghosts in a simple shear flow. *Physics of Fluids*. 1998; 10(8):1834–1845.
39. Pozrikidis C. Numerical simulation of the flow-induced deformation of red blood cells. *Annals of Biomedical Engineering*. 2003; 31(10):1194–1205. [PubMed: 14649493]
40. Liu Y, et al. Immersed electrokinetic finite element method. *International Journal for Numerical Methods in Engineering*. 2007; 71(4):379–405.
41. Peskin CS, Mcqueen DM. A 3-Dimensional Computational Method for Blood-Flow in the Heart . 1. Immersed Elastic Fibers in a Viscous Incompressible Fluid. *Journal of Computational Physics*. 1989; 81(2):372–405.

42. Peskin CS, Mcqueen DM. Modeling Prosthetic Heart-Valves for Numerical-Analysis of Blood-Flow in the Heart. *Journal of Computational Physics*. 1980; 37(1):113–132.
43. Peskin CS. The immersed boundary method. *Acta Numerica*. 2002; 11:479–517.
44. Saad Y, Schultz MH. Gmres - a Generalized Minimal Residual Algorithm for Solving Nonsymmetric Linear-Systems. *Siam Journal on Scientific and Statistical Computing*. 1986; 7(3): 856–869.
45. AlMomani T, et al. Micro-scale Dynamic Simulation of Erythrocyte–Platelet Interaction in Blood Flow. *Annals of Biomedical Engineering*. 2008; 36(6):905–920. [PubMed: 18330703]
46. Ariei L, Edelstein NA. Brownian simulation of many-particle binding to a reversible receptor array. *Journal of Computational Physics*. 1997; 132:260–275.
47. Breedveld V, et al. The measurement of the shear-induced particle and fluid tracer diffusivities in concentrated suspensions by a novel method. *Journal of Fluid Mechanics*. 1998; 375:297–318.
48. Marchioro M, Acrivos A. Shear-induced particle diffusivities from numerical simulations. *Journal of Fluid Mechanics*. 2001; 443:101–128.
49. Wang Y, Mauri R, Acrivos A. The transverse shear-induced liquid and particle tracer diffusivities of a dilute suspension of spheres undergoing a simple shear flow. *Journal of Fluid Mechanics*. 1996; 327:255–272.
50. Boryczko K, Dzwiniel W, Yuen DA. Dynamical clustering of red blood cells in capillary vessels. *Journal of Molecular Modeling*. 2003; 9(1):16–33. [PubMed: 12638008]
51. Farokhzad OC, et al. Targeted nanoparticle-aptamer bioconjugates for cancer chemotherapy in vivo. *Proceedings of the National Academy of Sciences*. 2006; 103(16):6315–6320.
52. Win KY, Feng S-S. In vitro and in vivo studies on vitamin E TPGS-emulsified poly(D,L-lactic-co-glycolic acid) nanoparticles for paclitaxel formulation. *Biomaterials*. 2006; 27(10):2285–2291. [PubMed: 16313953]
53. Pandey R, et al. Nanoparticle encapsulated antitubercular drugs as a potential oral drug delivery system against murine tuberculosis. *Tuberculosis*. 2003; 83(6):373–378. [PubMed: 14623168]
54. Decuzzi P, Ferrari M. The adhesive strength of non-spherical particles mediated by specific interactions. *Biomaterials*. 2006; 27(30):5307–5314. [PubMed: 16797691]
55. Lee J-H, et al. Effective viscosities and thermal conductivities of aqueous nanofluids containing low volume concentrations of Al₂O₃ nanoparticles. *International Journal of Heat and Mass Transfer*. 2008; 51(11–12):2651–2656.
56. Bea Woldhuis G-JT. concentration profile of blood platelets differs in arterioles and venules. *American Journal of Physiology-Heart and Circulatory Physiology*. 1992; 262(4):H1217–H1223.
57. Crowl LM, Fogelson AL. Computational model of whole blood exhibiting lateral platelet motion induced by red blood cells. *International Journal for Numerical Methods in Biomedical Engineering*. 2010; 26(3–4):471–487. [PubMed: 21152372]
58. Zhao R, J.N.M. Antaki JF. Drag-reducing polymers diminish near-wall concentration of platelets in microchannel blood flow. *Biorheology*. 2011; 47(3–4):193–203. [PubMed: 21084744]
59. Zhao R, et al. Micro-Flow Visualization of Red Blood Cell-Enhanced Platelet Concentration at Sudden Expansion. *Annals of Biomedical Engineering*. 2008; 36(7):1130–1141. [PubMed: 18418710]
60. Douglas JF, Steve Granick HEJ. A simple kinetic model of polymer adsorption and desorption. *Science*. 1993; 262(24):2010–2012. [PubMed: 17794964]
61. Park JJ, et al. Characterization of Non-Equilibrium Nanoparticle Adsorption on a Model Biological Substrate. *Langmuir*. 2010; 26(7):4822–4830. [PubMed: 20099807]
62. Haun JB, Hammer DA. Quantifying Nanoparticle Adhesion Mediated by Specific Molecular Interactions. *Langmuir*. 2008; 24(16):8821–8832. [PubMed: 18630976]
63. Thomas A, DD, Tan J, Muzykantov V, Liu Y. Characterization of Nanoparticle Transport and Distribution by Microfluidic Channels. 2011 in preparation,
64. Whitesides GM, et al. Soft lithography in biology and biochemistry. *Annual Review of Biomedical Engineering*. 2001; 3(1):335–373.

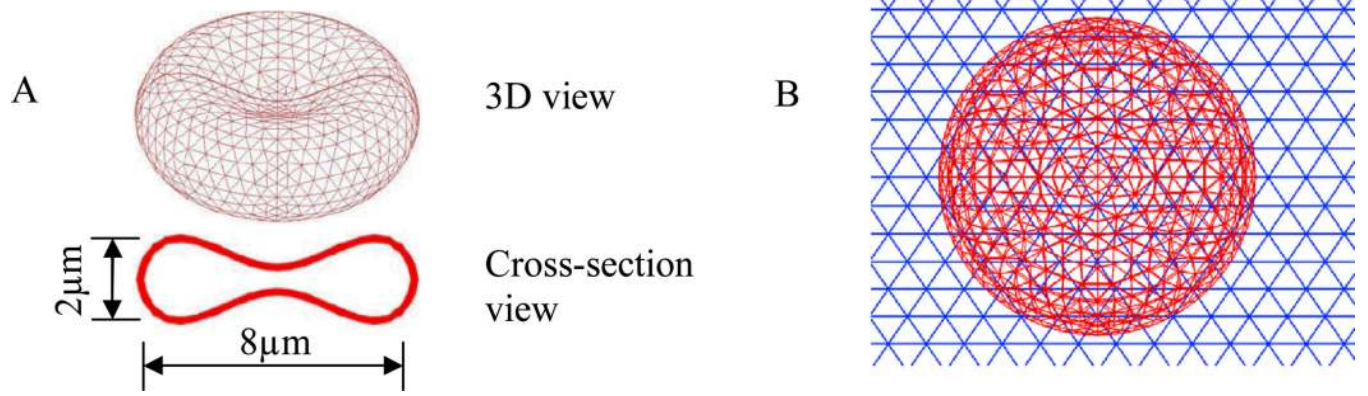


Figure 1.
(A) Geometry and mesh of RBC; (B) Mesh of RBC and fluid

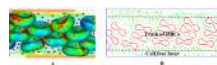


Figure 2.
(A) 3D simulation of nanoparticle-RBC interaction; (B) Cross-section view of nanoparticle-RBC interaction.

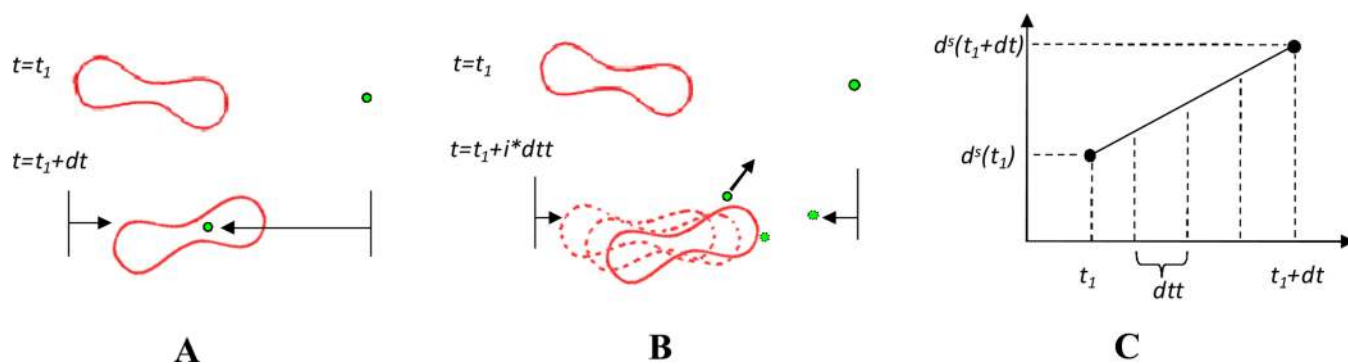


Figure 3. Illustration of the two time steps and mapping algorithms used in the simulation. (A) Overlapping happens when the same time step dt is used for both RBCs and NPs. (B) different time steps are used for RBCs (dt) and NPs (dtt) so that the overlapping is avoided. (C) Illustration of linear interpolation for RBC's intermediate positions.

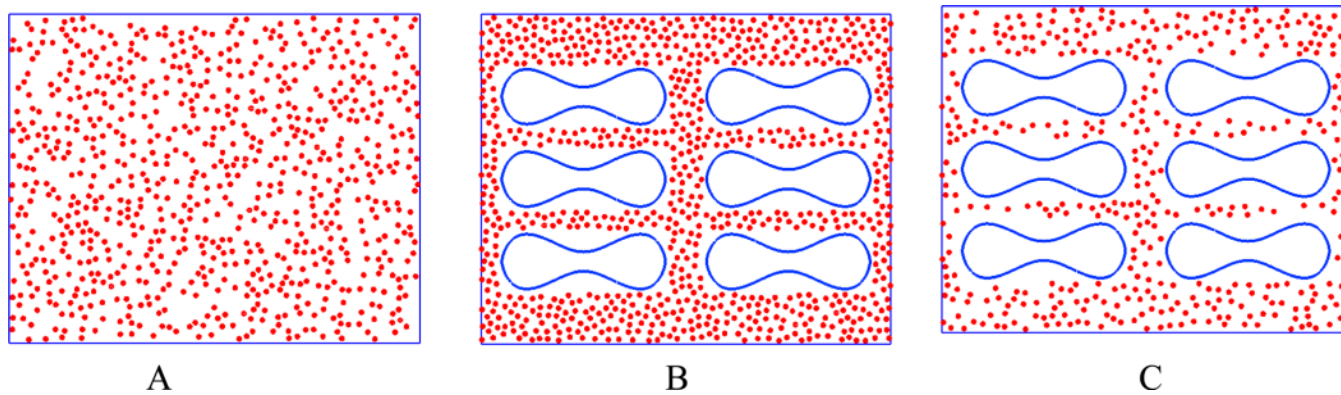


Figure 4. Illustration of three different simulation setups: (A) pure particles; (B) same NP dosage mixed with RBCs; (C) same effective particle concentration mixed with RBC s.

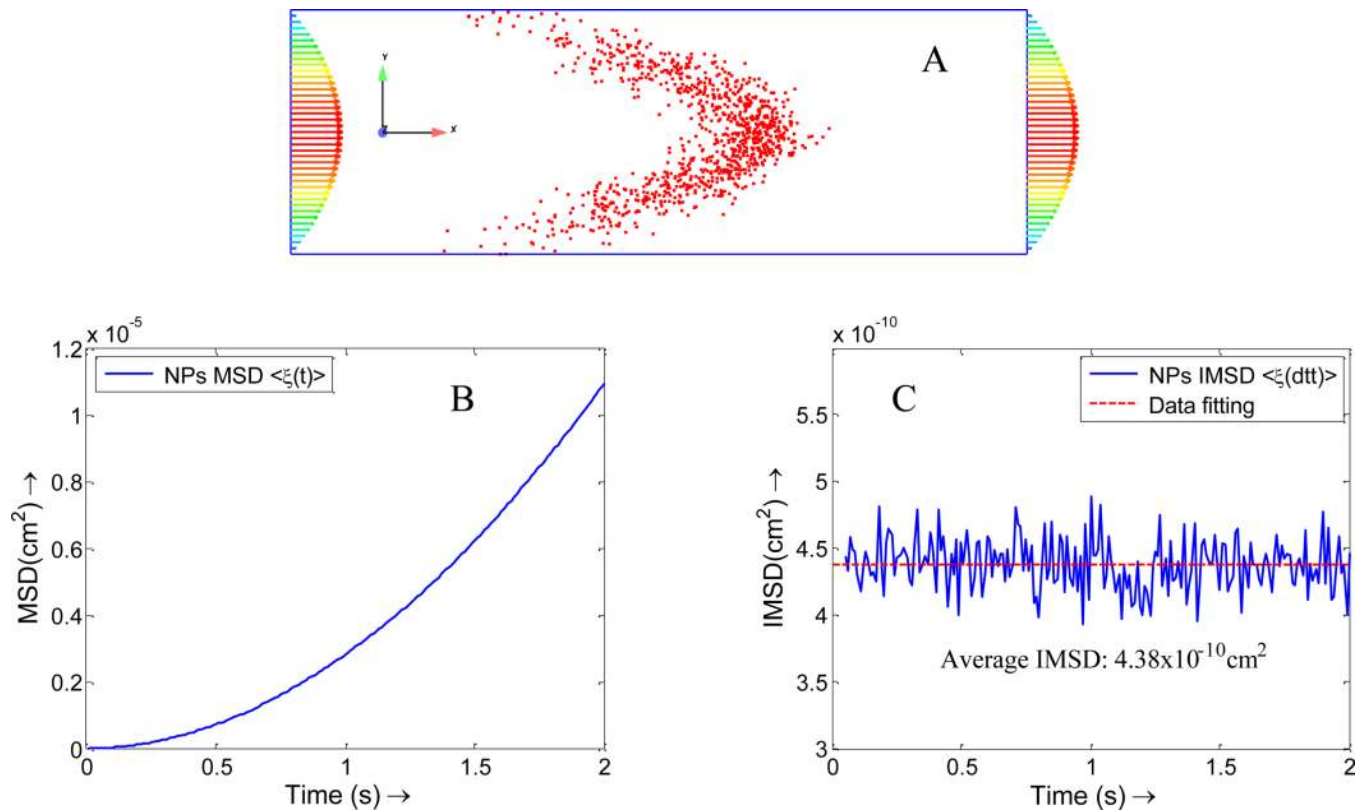


Figure 5. (A) Taylor-Aris effect for the NP diffusion in vessel. (B) Overall Mean square displacement (MSD) for NPs in flow direction, which is a quadratic function of time t ; (C) Instantaneous Mean Square Displacement (IMSD) for NPs in flow direction, the average instantaneous diffusion coefficient is about $2.2 \times 10^{-8} \text{cm}^2/\text{s}$ (here $dt=0.01\text{s}$, which is different from NP-RBC simulation case).

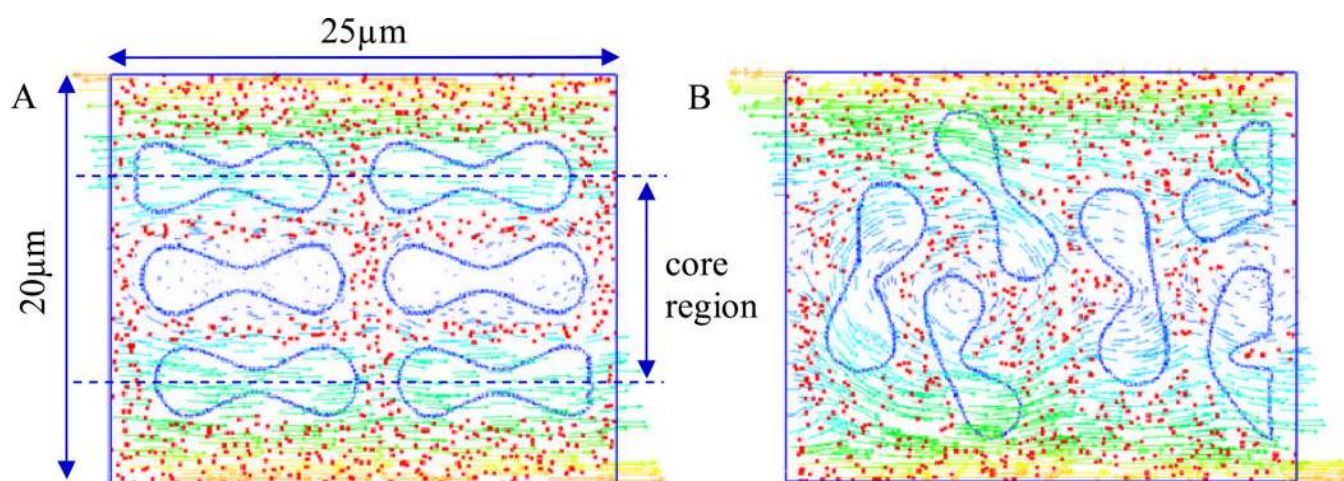


Figure 6. Simulation of RBCs and NPs interaction under a shear flow. (A) initial configuration of the model; (B) a snap shot of the model at 0.74 s .

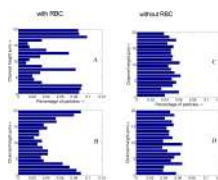


Figure 7. Nanoparticle distribution profile across the vessel. (A) initial NP distribution profile with RBCs; (B) NP distribution profile with RBCs at 1 s; (C) initial NP distribution profile without RBCs; (D) NP distribution profile without RBCs at 1 s.

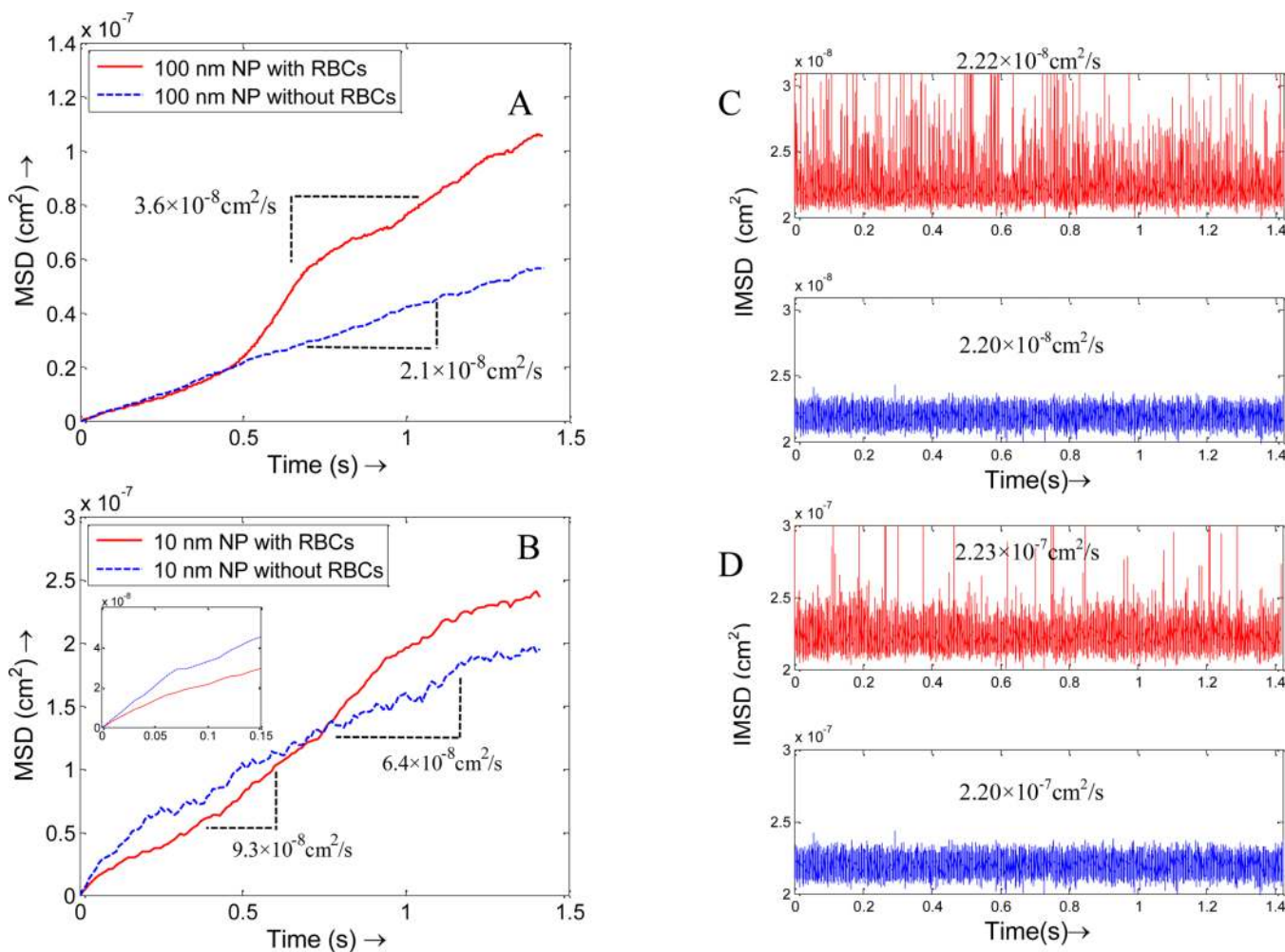


Figure 8.

The overall mean square displacements (MSD) of the particles with RBCs and without RBCs under a shear rate of 8 s^{-1} , which show that RBCs enhance the dispersion for both larger NPs and smaller NPs, but in slightly different ways. (A) NPs with size of 100 nm; (B) NPs with size of 10 nm, the zoom-in subplot show smaller NPs are trapped initially by RBCs. Instantaneous mean square displacement (IMSD) of the particles with RBCs and without RBCs under shear rate of 8 s^{-1} : (C) NPs with size of 100 nm; (D) NPs with size of 10 nm.

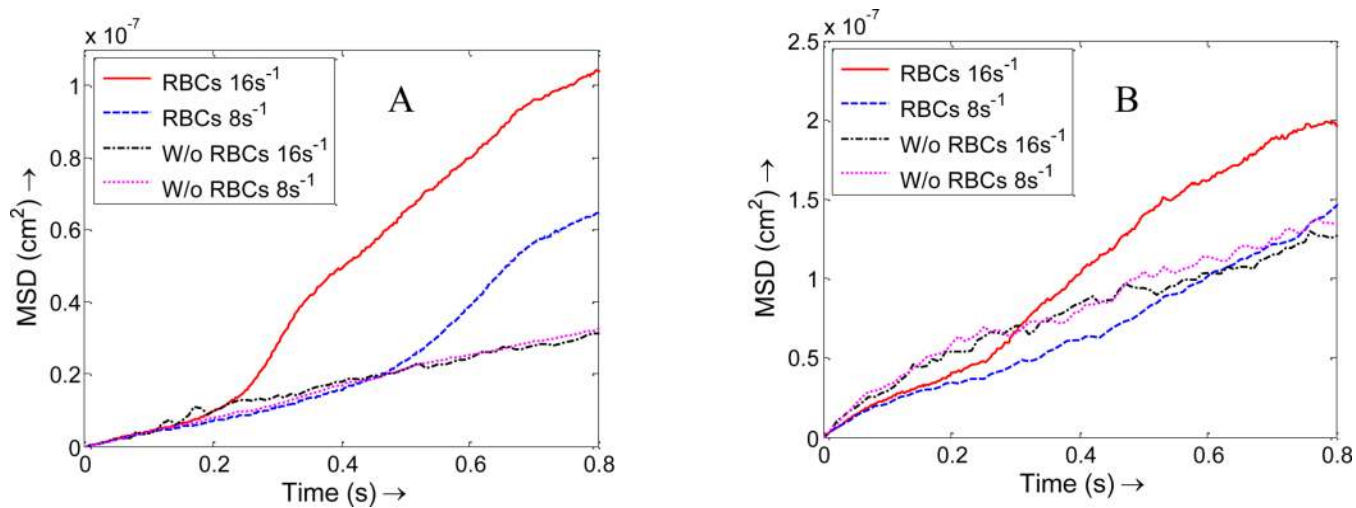


Figure 9. Mean square displacement of NPs under shear rates of 8 s^{-1} and 16 s^{-1} with RBCs and without RBCs. (A) 100 nm size of NPs; (B) 10 nm size of NPs.

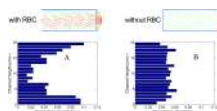


Figure 10. Particle distribution profile at time $t=7.5s$. (A) NPs with RBCs case; (B) NPs without RBCs.

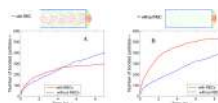


Figure 11.

(A) Nanoparticle binding time histories with and without RBCs of the same effective nanoparticle density; (B) Nanoparticle binding time histories with and without RBCs of the same NP dosage.

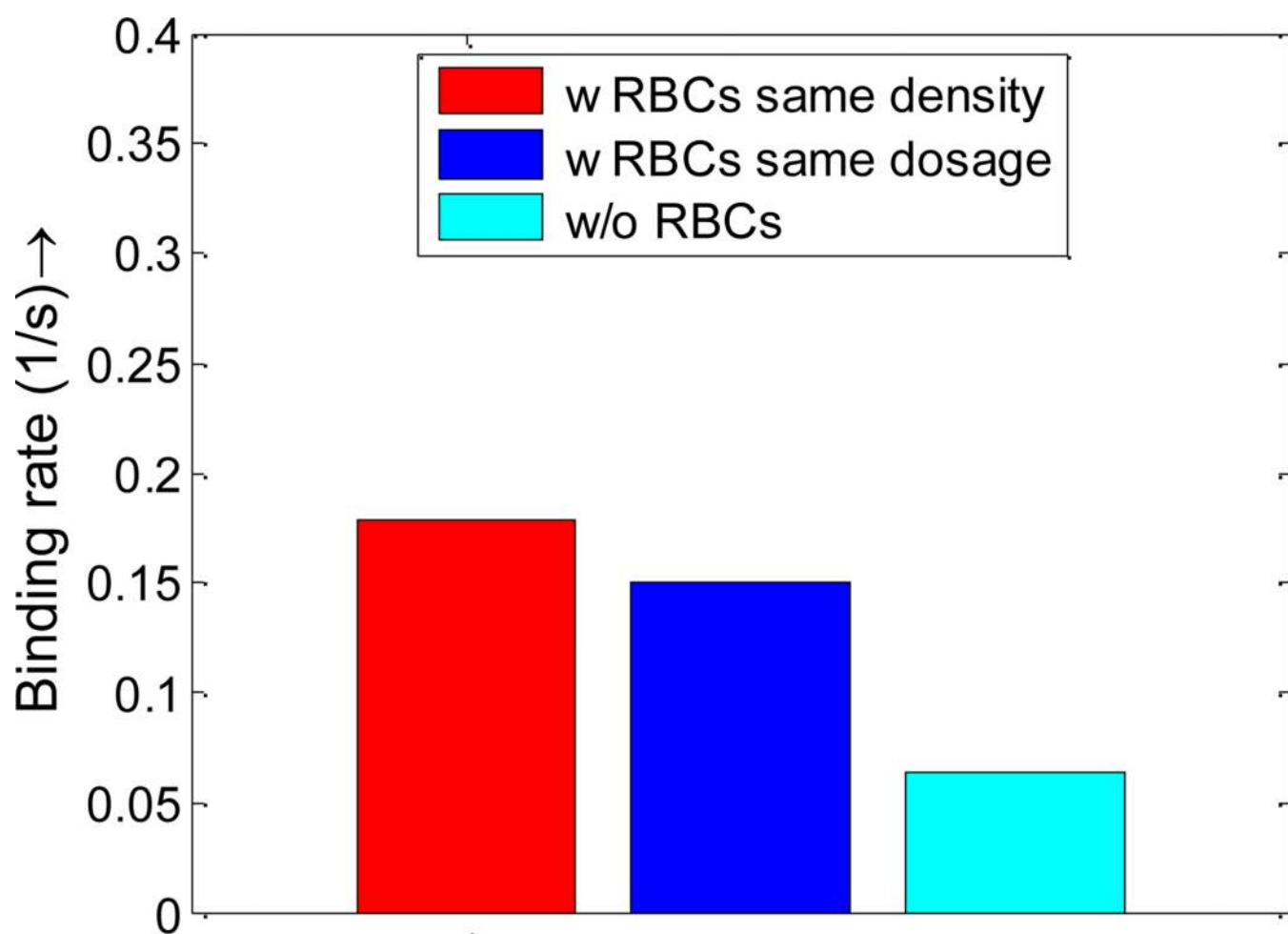


Figure 12. NPs binding rates with RBCs and without RBCs under same density and same dosage. Such increased binding rate is explained by the higher NP concentration in the cell-free-layer and larger dispersion rate.



Figure 13.
(A) Initial configuration of NPs and RBCs; (B) snapshot of NP distribution in capillary flow at time 1s with an average flow velocity $20 \mu\text{m/s}$.

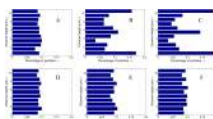


Figure 14. NPs distribution at $t=0s$, $0.5s$ and $1s$ when flowing with RBCs(A,B,C) and without RBCs(D,E,F) in capillary with diameter of $11\ \mu m$.

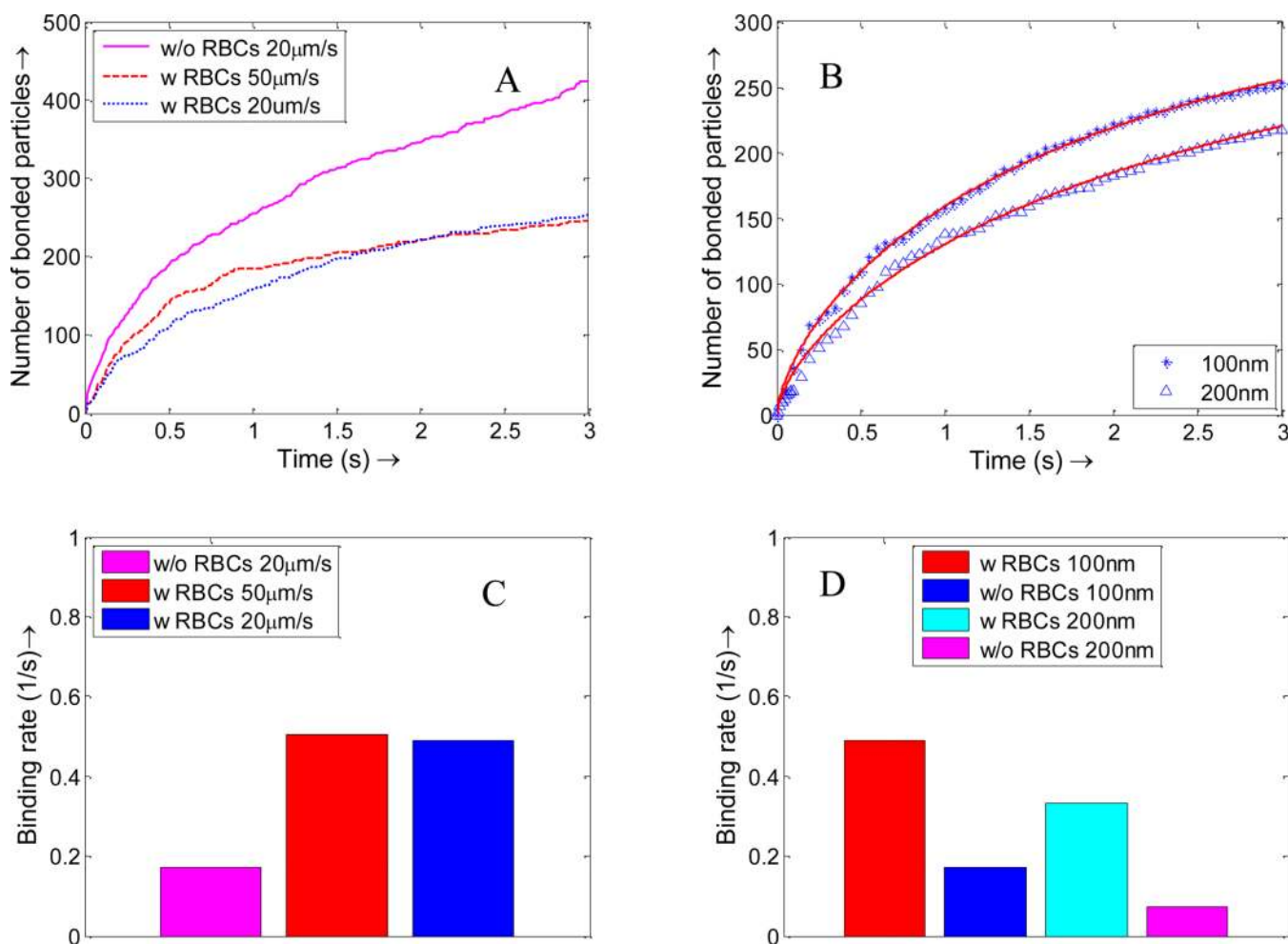


Figure 15.

(A) NPs binding time history with and without RBCs under different flow rates; (B) Binding time histories of NPs of different sizes, with and without RBCs, under a 20 $\mu\text{m/s}$ flow. The star and triangle represent simulation data, while the solid line is obtained by data fitting. Using the first order reaction model fitting, the binding rates for NPs of different sizes with RBCs and without RBCs under different flow speeds are obtained: (C) NP binding rate under different flow rates; (D) Binding rate for NPs of different sizes with flow rate of 20 $\mu\text{m/s}$.

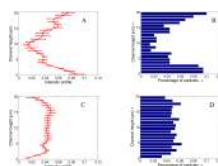
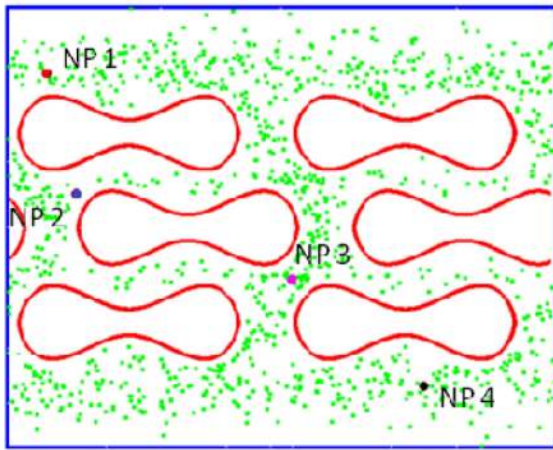
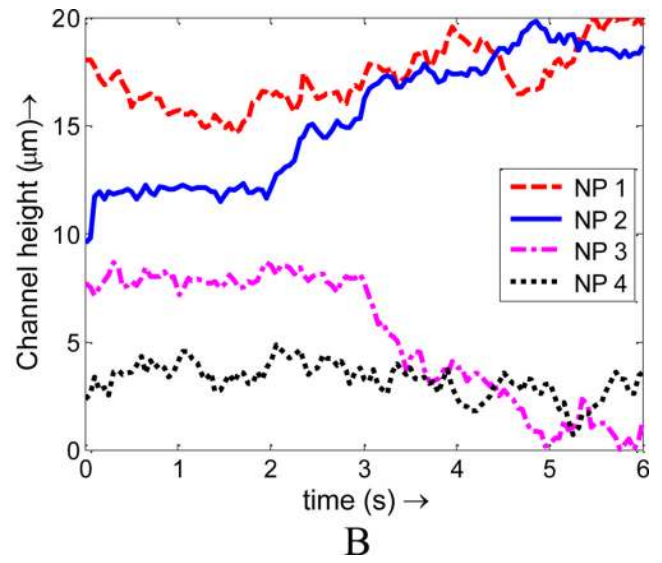


Figure 16. Fluorescence intensity across the channel in microfluidic tests, the error bar is plotted based on 10 runs of tests: (A) with RBCs; (C) without RBCs; (B) and (D): simulated NP distribution across the channel in the simulation with and without RBCs from Figure 10.



A



B

Figure 17.

(A) Initial positions of four NPs chosen at different locations; (B) Trajectory of NPs under the interaction of RBCs in capillary flow

Table 1

Parameters used in Lennard-Jones potential and Morse potential

Parameter	ϵ	σ	D_e	β	r_0
Value	10^{-15} J	200.0 nm	4.1×10^{-13} J	$2 \mu\text{m}^{-1}$	0.5 μm